in AML, ALL and CML. Similar events related to treatment with DNA topoisomerase II inhibitors? *Leukemia* 1997; **11**: 1571–4.
9 Tsuzuki M, Handa K, Yamamoto K *et al*. Chronic myeloid leukemia following chemotherapy with 5′-deoxy-5-fluorouridine for gastric cancer. *Intern. Med.* 2008; **47**: 1739–41.
10 Kuhn NZ, Tuan RS. Regulation of stemness and stem cell niche of mesenchymal stem cells: Implications in tumorigenesis and metastasis. *J. Cell. Physiol.* 2010; **222**: 268–77.

ADC Online First, published on November 25, 2013 as 10.1136/archdischild-2013-305037

Clinical and genetic aspects of hypophosphatasia in Japanese patients

Takeshi Taketani,[1,2] Kazumichi Onigata,[2] Hironori Kobayashi,[2] Yuichi Mushimoto,[2] Seiji Fukuda,[2] Seiji Yamaguchi[2]

▶ Additional material is published online only. To view please visit the journal online (http://dx.doi.org/10.1136/archdischild-2013-305037).

[1]Division of Blood Transfusion, Shimane University Hospital, Shimane, Japan
[2]Department of Pediatrics, Shimane University Faculty of Medicine, Shimane, Japan

Correspondence to
Dr Takeshi Taketani, Division of Blood Transfusion, Shimane University Hospital, 89-1, Enya, Izumo, Shimane 693-8501, Japan; ttaketani@med.shimane-u.ac.jp

Received 9 August 2013
Revised 23 September 2013
Accepted 1 November 2013

ABSTRACT

Objective We examined the clinical and genetic features of hypophosphatasia (HPP) in Japanese patients. HPP is a rare metabolic bone disorder of bone mineralisation caused by mutations in the liver/bone/kidney alkaline phosphatase (*ALPL*) gene, which encodes tissue-non-specific alkaline phosphatase isoenzyme.

Methods We retrospectively investigate the incidence and clinical features of 52 patients with paediatric HPP who were born between 1999 and 2010. Mutations of the *ALPL* gene were analysed in 31 patients.

Results The annual incidence of perinatal lethal HPP (PLH) was estimated to be 2–3/1 000 000 births. The most frequent clinical type was PLH followed by prenatal benign. In addition to bone symptoms, cerebral manifestations were frequently observed including convulsion, mental retardation, deafness and short stature with growth hormone deficiency. Respiratory failure was the most significant predictor of a poor prognosis for PLH. The first and second most frequent mutations in the *ALPL* gene were c.1559delT and c.T979C (p.F327L), respectively. The c.1559delT homozygous mutation was lethal with respiratory failure. Patients with the p.F327L compound heterozygous mutation had the different non-lethal type with short stature and a gradual improvement in ALP level and bone mineralisation.

Conclusions The most frequent clinical type was the PLH type with prognosis related to respiratory failure, biochemical/radiological changes and *ALPL* mutations. Cerebral manifestations frequently occurred. Genotype–phenotype correlations were associated with specific outcomes in the PLH type, whereas different clinical features were associated with the same genotype in the non-lethal type.

What is already known

- Hypophosphatasia (HPP) is characterised by defective bone and tooth mineralisation and reduced serum ALP activity.
- The clinical severity of HPP depends on the age of onset.
- The phenotypes of HPP are related to the residual enzyme activity of alkaline phosphatase (ALPL) mutations.

What this study adds

Japanese patients with hypophosphatasia (HPP) have many cerebral manifestations. The most frequent clinical type was the perinatal lethal HPP (PLH) type with prognosis was related to respiratory failure, biochemical/radiological changes and alkaline phosphatase (*ALPL*) mutations. Genotype–phenotype correlations were associated with specific outcomes in the PLH type, whereas different clinical features were associated with the same genotype in the non-lethal type.

INTRODUCTION

Hypophosphatasia (HPP) is a metabolic bone disorder caused by mutations in the liver/bone/kidney alkaline phosphatase (*ALPL*) gene, which encodes tissue-non-specific alkaline phosphatase.[1 2] This disease is characterised by defective bone and tooth mineralisation and reduced serum ALP activity.[1 2] According to several reports from Western populations, HPP patients exhibit autosomal dominant (AD) and autosomal recessive (AR) inheritance, while almost all HPP patients in the Japanese population are AR.[3–6] Patients with AR inheritance have a severe or mild clinical phenotype, whereas those with AD have a mild phenotype.[1–4] The clinical severity of HPP often depends on the age of onset.[2] The five clinical types of HPP are: (1) perinatal which is apparent at birth, (2) infantile from 1 to 6 months, (3) childhood type from the age of 6 months to 18 years, (4) odonto type, which is characterised by the premature loss of deciduous teeth by 5 years without apparent bone symptoms and (5) adult. The perinatal type is usually lethal because of a profound reduction in osteogenesis; half of the patients with the infantile type and all patients with the childhood type survive but experience premature loss of deciduous teeth as well as delayed walking and waddling, which reflect the degree of the skeletal disease.[1 2] However, some patients with prenatal onset, namely the prenatal benign type have ameliorated spontaneous skeletal defects and survive.[2 7 8] Low ALP activity contributes to elevated levels of ALP substrates, that is, pyridoxal 5′-phosphate, phosphoethanolamine (PEA) and inorganic pyrophosphate.[1] More than 260 types of *ALPL* mutations have been identified in HPP patients, and 80% of these are missense mutations according to the *ALPL* mutations database (http://www.sesep.uvsq.fr/03_hypo_mutations.php#mutations). The phenotypes of HPP patients are also closely related to the residual enzyme activity effects of *ALPL* mutations.[9 10] No curative therapy has been established for HPP. Currently, bone-targeted enzyme replacement therapy and cell

To cite: Taketani T, Onigata K, Kobayashi H, *et al. Arch Dis Child* Published Online First: [*please include* Day Month Year] doi:10.1136/archdischild-2013-305037

transplantation from bone marrow and other bone sources are under development.[11–15]

There are very few group-specific or country-specific reports on the clinical and genetic features of HPP in paediatric patients. However, the common *ALPL* mutations observed in Japanese patients, that is, homozygous mutation of c.1559delT and compound heterozygous mutation of c.T979C (p.F327L) have been shown to be associated with relatively lethal and mild types of HPP, respectively.[4–6] Therefore, our study examined the clinical and genetic aspects of HPP in Japanese children.

METHODS

Clinical survey of HPP patients

A questionnaire was sent to approximately more than 500 paediatric medical institutes (95%) throughout Japan to determine the incidence of patients with paediatric HPP born between 1999 and 2010. A thorough review of institutions reporting HPP patients involved the verification of clinical types and features, serum ALP and urine PEA levels in a spot urine collection and radiographic exam information. Clinical features were reviewed from onset to initiation of investigation (June 2010), while biochemical and radiographic tests were performed only at diagnosis. Short stature was defined as −2 SD of height. The diagnostic criteria of growth hormone deficiency (GHD) were as follows: (1) height less than −2.5 SD, (2) insulin-like growth factor-1 less than 200 ng/mL and (3) GH release deficiency in GH secretion test with insulin, arginine or L-3,4-dihydroxyphenylalanine. Assessment of mental retardation was performed by: developmental quotient scores, the Enjoji scale of infant analytical development or IQ. Five clinical types were defined as follows: perinatal lethal HPP (PLH), prenatal benign HPP (PBH), infantile, childhood and odonto. We defined the PLH type as occurrence of a respiratory failure within 1 month after birth and the prenatal benign type as no respiratory failure because other clinical symptoms could not be differentiated between the PLH and PBH types.

ALPL gene analysis

After informed consent was obtained, *ALPL* gene analysis of 31 patients in 52 patients was performed. DNA was extracted from peripheral blood samples and the entire *ALPL* coding region was sequenced by PCR to analyse mutations (Ensembl/Havana merged gene: ENSG00000162551). DNA (50 ng) solution was amplified by PCR in a total volume of 20 µL with 10 mM Tris–HCl (pH 8.3), 50 mM KCl, 1.5 mM $MgCl_2$, 0.001% (wt/vol) gelatin, 5% dimethyl sulfoxide, 250 µM of each deoxynucleotide triphosphates, 2.5 units Taq polymerase (AmpliTaq Gold; Applied Biosystems, Foster City, California, USA) and 10 pmol of each primer. The primers used in these analyses are shown in online supplementary table S1. PCR amplification was performed using a DNA thermal cycler (Applied Biosystems) under the following conditions: initial denaturation at 95°C for 9 min, 35 cycles at 95°C for 30 s, 60°C for 30 s and 72°C for 1 min, followed by a final elongation at 72°C for 7 min. The PCR products were sequenced by the fluorometric method using the BigDye terminator cycle sequencing kit (Applied Biosystems).

RESULTS

Incidence

Paediatric doctor of appropriately 70% hospitals in which we sent the questionnaire replied. The survey collected data from 52 patients. The frequencies of patients with PLH, prenatal PBH, infantile, childhood and odonto type HPP were 21, 14, 5, 9 and 3, respectively. There was neither adult type nor mild HPP with AD fashion. The annual incidence was 2–10 patients each year. The male to female ratio was 33:19 (p=0.055). The number of sporadic and familial patients was 46 and 6, respectively. The incidence of patients with HPP tended to be geographically constrained. In particular, patients were significantly more prevalent in Honshu, the main island of Japan than other islands including Hokkaido, Shikoku, Kyushu and Okinawa (p=0.03).

Clinical type-related characteristics

PLH and PBH types

All patients with PLH and PBH types (n=35) underwent the fetal ultrasonographic examination. Short extremities or deformed limbs and hydramnios were detected in 19/35 of fetuses (54%) (table 1, figure 1). Out of 19 patients with an abnormal fetal echo test, 12 were PLH and 7 PBH. The abnormal ultrasound findings were detected at 20–30 weeks of

Table 1 Clinical and radiographic characteristics of hypophosphatasia

	Perinatal lethal (21)	Prenatal benign (14)	Infantile (5)	Childhood (9)
Clinical findings				
Shortening or deformity of the extremities	15	13	0	4
Bone fracture	3	4	1	0
Respiratory failure	21	0	1	0
Convulsion	9	0	1	2
Enlargement of the anterior fontanelle	4	2	4	0
Renal calcification	3	0	0	0
Short stature	5	8	2	6
Failure to thrive	9	4	5	1
Premature loss of deciduous teeth	5	4	0	3
Mental retardation	5	2	1	3
Premature synostosis of the skull	2	0	2	0
Deafness	5	0	0	0
Radiographic findings				
Hypomineralisation	21	4	5	0
Loss of bone	7	2	0	0
Deformity of long bones	13	12	0	4
Flared metaphyses	13	7	5	1
Hypolucent mid-metaphyses	5	5	1	0
Osteochondral spurs	0	0	0	0
Narrow thorax	19	1	4	0
Biochemical tests				
ALP (IU/L)	20.1	74.8	98	145
Urine PEA (µmol/mg Cr)	7021	2261	1605	873

The alkaline phosphatase (ALP) and urine PEA values are averages. Numbers in parentheses indicate the number of patients. Numbers in brackets indicate biochemical value of ALP and urine PEA. In Japan, the normal blood ALP range is as follows: median 490 IU/L (range=59–921) from birth to 1 month; median 617 IU/L (range=199–1035) during 2–5 months; median 471 IU/L (range=180–762) from 6 months to 1 year. The lower cut-off level during years 1–7 was 170 IU/L. The normal urine PEA range is 31–110 µmol/mg Cr.
PEA, phosphoethanolamine.

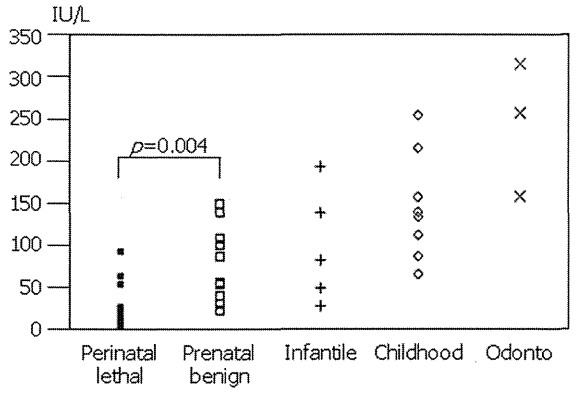

Figure 1 The alkaline phosphatase (ALP) levels of different clinical types.

gestation. The age when diagnosis was confirmed ranged from 0 to 21 days after birth. Two patients were diagnosed 2 weeks after birth because of life-threatening conditions. The main symptoms in both types were short extremities, deformed limbs and bone fractures, short stature, failure to thrive, mental retardation and constipation; respiratory failure, vitamin B6-dependent convulsion, deafness, renal calcification and premature synostosis of the skull occurred only in PLH. Most patients with PLH developed tracheobronchial spasm due to tracheomalacia or bronchomalacia and pulmonary hypertension due to hypercapnia or pulmonary dysfunction. The former condition repeatedly induced severe cyanotic attacks and hypoxic brain damage was recorded. Two of 14 patients with PBH presented with short stature complicated by GHD.

The ALP level was significantly lower in PLH compared with PBH (p=0.0004) (figure 1), while the urine PEA titre was significantly higher in the former (p=0.0035). Radiographic examination showed that significant hypomineralisation and narrow thorax were more frequent in PLH than in PBH (p<0.0001). Osteochondral spurs were not found. In PBH, the ALP titre and urine PEA tended to be gradually increased and decreased, respectively. The hypomineralisation also improved gradually.

According to the prognosis, the median time of death was 4 months (range=0–68 months) in PLH type (figure 2); however, four patients with the PLH type kept survived over 3 years. The main cause of death was respiratory failure. The ALP concentration was significantly lower in PLH type than in PBH (p=0.00187). Respiratory failure (p=0.0001), hypomineralisation (p=0.0008), bone loss (p=0.0021) and narrow thorax

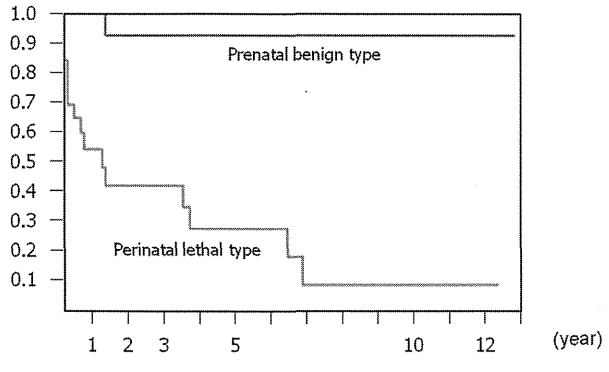

Figure 2 Overall survival rates with respiratory failure (Kaplan–Meier method). The red and green lines indicate patients with and without respiratory failure, respectively.

(p=0.0091) significantly correlated with a poor prognosis, whereas bone shortening/deformity, convulsion and failure to thrive did not. All patients with respiratory failure died within 60 months, with one exception, where respiratory failure developed from a respiratory distress syndrome caused by a premature birth. Another patient of PBH died of viral cardiomyopathy.

Infantile type

No abnormalities were found during the perinatal period in five cases with the infantile form. The age of diagnosis was 2–4 months. All five patients exhibited failure to thrive, hypercalcaemia, hypomineralisation and flared metaphyses which resulted in rickets. For the follow-up period (3–10 years), premature loss of deciduous teeth was not recorded in any cases at the age of 5 years. Only one patient had respiratory failure resulting in death. Two living patients presented with short stature and ambulation difficulty.

Childhood type

The median age was 3 years (range = 10 months to 5 years) at diagnosis. Short extremities, short stature and premature loss of deciduous teeth existed at diagnosis. Mental retardation and convulsion were also recorded. Long bone deformities were found in four patients during radiographic examination. Hypomineralisation and flared metaphyses were not present. All nine patients survived. Three of the six patients with short stature were treated with GH.

Odonto type

The age of diagnosis was 2–4 years. The only clinical symptom was a premature loss of deciduous teeth in all three patients. The median ALP level was 200 IU/L.

Gene analysis

ALPL mutations were identified in 31 patients: 19 perinatal, 5 infantile, 5 childhood and 2 odonto types (table 2). The remaining

Table 2 Genetic analysis of the *ALPL* gene

Clinical types	Genotype	Number of patients
Perinatal lethal type	c.1559delT/c.1559delT	7
	c.1559delT/p.N190del	1
	c.1559delT/p.H324R	1
	c.1559delT/p.G426S	1
	c.1559delT/p.R433C	1
	p.R223Q/p.R272C	1
Prenatal benign type	c.1559delT/p.F327L	2
	p.F327L/p.R428X	1
	p.F327L/p.G439R	1
	p.F327del/p.R184W	1
	p.A40V/p.E191G	2
Infantile type	c.1559delT/p.L299P	2
	c.1559delT/p.F327L	1
	c.1559delT/p.Y436C	1
	p.K224E/p.G426C	1
Childhood type	c.1559delT/ pF327L	3
	p.F327L/p.G339R	1
	p.F327L/p.A111T	1
Odonto type	c.1559delT/p.R136H	2

ALPL, alkaline phosphatase.

21 patients did not receive genetic testing. Two mutant alleles were identified in 31 patients and no heterozygous mutations were found, suggesting that most Japanese HPP cases are the result of AR inheritance. All parents were found to be carriers in the genetic analysis of the parents of 15 patients. Mutations in c.1559delT (29 alleles) and p.F327L (10 alleles) were the frequent mutations. The most frequent Japanese HPP genotype was a homozygous mutation (c.1559delT/c.1559delT), which was observed in seven patients, while the compound heterozygous mutation of c.1559delT/p.F327L was found in six patients. No homozygous mutation of p.F327L was detected. Interestingly, patients with p.F327L were all types except for the PLH type. There is no distortion of the distribution of mutations depending on the island the patients originate.

All seven patients with c.1559delT/c.1559delT had the PLH type with respiratory failure. Five of seven patients with the mutation died, whereas the other two received mechanical ventilation. The frequency of hypominiralisation ($p=0.0299$) and respiratory failure ($p=0.0189$) were significantly higher and the ALP level was significantly lower (28.7 vs 118.4 IU/L, $p=0.0098$) in patients with the homozygous mutation than in patients with other genotypes. Two of the six patients with the compound heterozygous mutation (c.1559delT/p.F327L) had PBH, one had the infantile type and three had the childhood type. All six patients with this genotype survived without serious sequelae but had short stature. Interestingly, siblings of these patients with this genotype had different clinical features. The oldest sibling had the childhood type and a short stature caused by bone deformity, whereas the youngest sibling had PBH, an immunoglobulin A nephropathy and a short stature which was caused by bone deformity and GHD.

DISCUSSION

This retrospective study investigated the clinical and genetic features of HPP in Japanese patients. The epidemiological study found that the perinatal lethal type was the most frequent and was more common in males than in females. The low number of patients with the infantile and childhood types as well as no patients with adult type and mild HPP with AD fashion may have been because HPP remains undiagnosed due to low awareness of HPP. In Japan, the annual incidence of PLH was estimated as about 2–3 patients/1 000 000 births, that is, one case in 300 000–500 000 births with a Japanese birth rate of 1.1 million/year. In Canada, the prevalence in the general population of the most severe forms of HPP is estimated to be ~1:100 000.[16] A molecular-based estimation of the prevalence of HPP in the European population estimated the prevalence of severe HPP and moderate HPP as 1/300 000 and 1/6370, respectively.[3] In the Japanese population, the prevalence of the 1559delT homozygous mutation in the *ALPL* gene, which is a common mutation that causes the perinatal lethal form, was estimated to be not less than 1/900 000.[6] Michigami *et al*[4] reported that c.1559delT represents 40.9% of severe alleles. This mutation was not found in other countries, suggesting that c.1559delT may be a founder mutation in the Japanese population.

Some of the perinatal type cases were diagnosed with HPP during the early gestational period based on ultrasound examination and a positive familial history. However, ultrasound abnormalities early in pregnancy are not necessarily diagnostic for perinatal forms of HPP[8] and may have resulted in elective abortion. Some fetal deaths may also have been the result of HPP. The current retrospective survey was not exhaustive, which is why the number of perinatal type cases may have been underestimated. Thus, a nationwide prospective survey is required to determine the actual incidence of HPP.

Compared with previous reports of HPP clinical characteristics in Western populations,[1 2] the frequency of mental retardation, deafness and short stature were more frequent in Japanese HPP patients, while convulsion was approximately the same. Mental retardation was observed in all types, even when patients did not present complications from hypoxic damage due to respiratory disturbance. The auditory tests were normal at birth, suggesting that deafness was acquired after birth and was not congenital. It is possible that the acquisition of deafness may be exacerbated by hypomineralisation of the ear ossicles. However, auditory brainstem response audiometry showed that the brainstem or cerebral cortex was damaged (data not shown). Short stature was also observed in all HPP types. Interestingly, approximately half of the patients with a short stature had GHD, rather than mineralisation dysfunctions or bone deformities. GHD in all patients was GH release deficiency in GH secretion test with insulin, arginine or L-DOPA, demonstrating that GH-secretion by the pituitary gland was decreased. ALP, present in the neuronal membrane, interacts with the synapses that are involved in neurotransmitter synthesis, synaptic stabilisation and myelin pattern formation; however, there are no reports of GHD in knockout mice.[17–20] Thus, ALP may play a role in developmental plasticity and activity-dependent cortical functions. A study in mice also showed that ALP dysfunction compromises myelination and synaptogenesis in the brain.[20] This suggests that cerebral impairment, including convulsion, mental retardation, deafness and GH deficiency, might be dependent on the severity of the ALP activity as well as the differences in the genetic and ethnic backgrounds of patients.

We designated patients with or without respiratory failure as PLH or PBH, respectively, because prognosis of respiratory failure was worse in the survey. Convulsion, renal calcification, premature synostosis of the skull and deafness were exclusive characteristics of the PLH type and were not poor prognostic predictors. Convulsion may be the best predictor of poor outcome because the follow-up period is short. Patients with the PLH type had significantly lower ALP levels and higher urine PEA levels compared with those with the PBH type. However, ALP and PEA absolute levels did not define the outcome because the cut-off value of ALP and PEA could not be identified. The radiological findings showed that bone mineralisation, flared metaphyses and a narrow thorax were significantly more frequent in the PLH type compared with the PBH type. Interestingly, ALP levels and bone mineralisation gradually increased in the benign type, suggesting that biochemical and radiographic changes need to be assessed over time. All patients with the c.1559delT homozygous mutation had the PLH type, whereas patients with p.F327L had the other types of HPP. Previous reports demonstrated that c.1559delT homozygous and p.F327L heterozygous mutations are associated with lethal and mild types, respectively.[4 5] These suggest that accurate prognosis of Japanese patients with HPP may depend on respiratory condition, biochemical/radiological changes and genetic mutation.

Interestingly, six patients who carried the c.1559delT/p.F327L compound heterozygous mutation were divided into three clinical types: PBH type, infantile type and childhood type. The different onset ages in patients with the same genotype were probably attributable to their initial symptoms. The primary presentation was a long bone deformity based on a fetal echo examination for patients with the PBH type. A bone

fracture was detected initially in patients with the infantile type. Patients with the childhood type were diagnosed based on their short stature or the premature loss of their deciduous teeth. The ALP level increased gradually and bone mineralisation improved gradually in the PBH and infantile types. Short stature was observed in all patients. All patients survived without severe sequelae. Wenkert *et al*[8] also reported that prenatal benign type severity post-natally spanned the 'infantile' to 'odonto' HPP phenotypes and that discordance for prenatal benign type occurred between siblings despite identical *ALPL* mutations. Ozono *et al*[21] proposed a molecular mechanism for the PBH type, suggesting greater expression of the allele harbouring the milder *ALPL* allele defect. The residual enzyme activity effects of *ALPL* mutations, c.1559delT and p.F327L, were none and 70%, respectively.[4] This suggests that patients with c.1559delT/p.F327L compound heterozygous mutations were at different ages at diagnosis, but have experienced the same good clinical course. Further biochemical and physiological investigation would need to clarify why patients with compound heterozygous mutations, c.1559delT/p.F327L, ameliorate.

CONCLUSIONS

This retrospective study investigated the clinical and genetic features of Japanese HPP patients. The incidence of PLH was estimated to be approximately 2–3/1 000 000 births. The most frequent clinical type was PLH, followed by PBH. The Japanese phenotype was frequent central nerve dysfunction including convulsions, mental retardation, deafness and short stature with GHD. We found that lifetime prognosis for HPP was related to respiratory failure, biochemical/radiological changes and *ALPL* mutations. Genotype–phenotype correlations were associated with specific outcomes, although different clinical features with non-lethal type had the same genotype.

Acknowledgements We thank all the Japanese attending physicians for kindly providing the clinical data of patients. We also thank Ms Midori Furui, Mayumi Nagase, Mayumi Naito, Rie Eda and Miho Hattori for analysis of the clinical data and support during molecular analysis.

Contributors TT conceptualised and designed the study, drafted the initial manuscript and approved the final manuscript as submitted. KO managed and designed the study, reviewed and revised the manuscript and approved the final manuscript as submitted. HK carried out the initial analyses, reviewed and revised the manuscript and approved the final manuscript as submitted. YM collected the clinical data and carried out the initial analyses, reviewed and revised the manuscript and approved the final manuscript as submitted. SF performed the genetic analysis of the ALPL gene, reviewed and revised the manuscript and approved the final manuscript as submitted. SY managed and designed the study, reviewed and revised the manuscript and approved the final manuscript as submitted.

Funding This study was supported by the Project for Realisation of Regenerative Medicine, Ministry of Education, Culture, Sports, Science and Technology; and Research on Regenerative Medicine for Clinical Application, Ministry of Health, Labor and Welfare.

Competing interests None.

Patient consent Obtained.

Ethics approval Study approved by the Institutional Review Board.

Provenance and peer review Not commissioned; externally peer reviewed.

REFERENCES

1 Whyte MP. Physiological role of alkaline phosphatase explored in hypophosphatasia. *Ann N Y Acad Sci* 2010;1192:190–200.
2 Mornet E. Hypophosphatasia. *Best Pract Res Clin Rheumatol* 2008;22:113–27.
3 Mornet E, Yvard A, Taillandier A, *et al*. A molecular-based estimation of the prevalence of hypophosphatasia in the European population. *Ann Hum Genet* 2011;75:439–45.
4 Michigami T, Uchihashi T, Suzuki A, *et al*. Common mutations F310L and T1559del in the tissue-nonspecific alkaline phosphatase gene are related to distinct phenotypes in Japanese patients with hypophosphatasia. *Eur J Pediatr* 2005;164:277–82.
5 Ozono K, Michigami T. Hypophosphatasia now draws more attention of both clinicians and researchers: a Commentary on prevalance of c. 1559delT in ALPL, a common mutation resulting in the perinatal (lethal) form of hypophosphatasias in Japanese and effects of the mutation on heterozygous carriers. *J Hum Genet* 2011;56:174–6.
6 Watanabe A, Karasugi T, Sawai H, *et al*. Prevalence of c.1559delT in ALPL, a common mutation resulting in the perinatal (lethal) form of hypophosphatasia in Japanese and effects of the mutation on heterozygous carriers. *J Hum Genet* 2011;56:166–8.
7 Brun-Heath I, Chabrol E, Fox M, *et al*. A case of lethal hypophosphatasia providing new insights into the perinatal benign form of hypophosphatasia and expression of the ALPL gene. *Clin Genet* 2008;73:245–50.
8 Wenkert D, McAlister WH, Coburn SP, *et al*. Hypophosphatasia: nonlethal disease despite skeletal presentation in utero (17 new cases and literature review). *J Bone Miner Res* 2011;26:2389–98.
9 Zurutuza L, Muller F, Gibrat JF, *et al*. Correlations of genotype and phenotype in hypophosphatasia. *Hum Mol Genet* 1999;8:1039–46.
10 Mornet E. Hypophosphatasia: the mutations in the tissue-nonspecific alkaline phosphatase gene. *Hum Mutat* 2000;15:309–15.
11 Nishioka T, Tomatsu S, Gutierrez MA, *et al*. Enhancement of drug delivery to bone: characterization of human tissue-nonspecific alkaline phosphatase tagged with an acidic oligopeptide. *Mol Genet Metab* 2006;88:244–55.
12 Whyte MP, Greenberg CR, Salman NJ, *et al*. Enzyme-replacement therapy in life-threatening hypophosphatasia. *N Engl J Med* 2012;366:904–13.
13 Whyte MP, Kurtzberg J, McAlister WH, *et al*. Marrow cell transplantation for infantile hypophosphatasia. *J Bone Miner Res* 2003;18:624–36.
14 Cahill RA, Wenkert D, Perlman SA, *et al*. Infantile hypophosphatasia: transplantation therapy trial using bone fragments and cultured osteoblasts. *J Clin Endocrinol Metab* 2007;92:2923–30.
15 Tadokoro M, Kanai R, Taketani T, *et al*. New bone formation by allogeneic mesenchymal stem cell transplantation in a patient with perinatal hypophosphatasia. *J Pediatr* 2009;154:924–30.
16 Fraser D. Hypophosphatasia. *Am J Med* 1957;22:730–46.
17 Fonta C, Négyessy L, Renaud L, *et al*. Areal and subcellular localization of the ubiquitous alkaline phosphatase in the primate cerebral cortex: evidence for a role in neurotransmission. *Cereb Cortex* 2004;14:595–609.
18 Fonta C, Negyessy L, Renaud L, *et al*. Postnatal development of alkaline phosphatase activity correlates with the maturation of neurotransmission in the cerebral cortex. *J Comp Neurol* 2005;486:179–96.
19 Négyessy L, Xiao J, Kántor O, *et al*. Layer-specific activity of tissue non-specific alkaline phosphatase in the human neocortex. *Neuroscience* 2011;172:406–18.
20 Hanics J, Barna J, Xiao J, *et al*. Ablation of TNAP function compromises myelination and synaptogenesis in the mouse brain. *Cell Tissue Res* 2012;349:459–71.
21 Ozono K, Yamagata M, Michigami T, *et al*. Identification of a novel missense mutations (Phe310Leu and Gly439Arg) in a neonatal case of hypophosphatasia. *J Clin Endocrinol Metab* 1996;81:4458–61.

ADC

Clinical and genetic aspects of hypophosphatasia in Japanese patients

Takeshi Taketani, Kazumichi Onigata, Hironori Kobayashi, et al.

Arch Dis Child published online November 25, 2013
doi: 10.1136/archdischild-2013-305037

Notes

Journal of Bioscience and Bioengineering
VOL. 116 No. 3, 380–385, 2013

www.elsevier.com/locate/jbiosc

Actin-based biomechanical features of suspended normal and cancer cells

Seyed Mohammad Ali Haghparast,[1] Takanori Kihara,[1,*] Yuji Shimizu,[1] Shunsuke Yuba,[2] and Jun Miyake[1]

Department of Mechanical Science and Bioengineering, Graduate School of Engineering Science, Osaka University, 1-3 Machikaneyama, Toyonaka, Osaka 560-8531, Japan[1] and Health Research Institute, National Institute of Advanced Industrial Science and Technology (AIST), 3-11-46 Nakoji, Amagasaki, Hyogo 661-0974, Japan[2]

Received 30 November 2012; accepted 5 March 2013
Available online 6 April 2013

The mechanical features of individual cells have been regarded as unique indicators of their states, which could constantly change in accordance with cellular events and diseases. Particularly, cancer progression was characterized by the disruption and/or reorganization of actin filaments causing mechanical changes. Thus, mechanical characterization of cells could become an effective cytotechnological approach for early detection of cancer. To develop mechanical cytotechnology, it would be necessary to clarify the mechanical properties in various cell adhesion states. In this study, we investigated the surface mechanical behavior of cancer and normal cells in the adherent and suspended states using atomic force microscopy. Adherent normal stromal cells showed high surface stiffness due to developed actin cap structures on their apical surface, whereas cancer cells did not have developed filamentous actin structures, and their surface stiffness was low. Upon cell detachment from the substrate, filamentous actin structures of adherent normal stromal cells reorganized to the cortical region and their surface stiffness decreased consequently however, the stiffness of suspended normal cells remained higher than that of cancer cells. These suspended state actin structures were similar, regardless of the cell type. Furthermore, the mechanical responses of the cancer and normal stromal cells to perturbation of the actin cytoskeleton were different, suggesting distinct regulatory mechanisms for actin cytoskeleton in cancer and normal cells in both adherent and suspended states. Therefore, cancer cells possess specific mechanical and actin cytoskeleton features different from normal stromal cells.

[**Key words:** Mechanical features; Atomic force microscopy; Suspended state; Cancer cell; Actin cytoskeleton; Mechanical cytotechnology]

Alterations in biological activities and transformation of cell states often entail a change in the mechanical behavior of cells. In particular, alterations in cell stiffness/elasticity have emerged as a marker for cellular phenotypic events and diseases. During optic-cup morphogenesis, a change in the stiffness of the retinal epithelium is important for the formation of neural retinal tissue (1). Malignant cancer cells exhibit lower stiffness than normal cells (2–4). Mechanical properties are largely attributable to the cytoskeleton components, especially actin microstructures which together are referred to as actin cytoskeleton (5–9). The above-mentioned stiffness alterations reflect the remodeling process of the actin and other cytoskeletal elements in the respective cellular events and disease states. Particularly, the actin cytoskeleton remodeling plays an important role in the life cycle of a cancer cell. Actin depolymerization and disrupted stress fibers, marked by a shift from F-actin to G-actin, occur in the early stages of malignant transformation (10,11). Besides, abnormal F-actin distribution and dynamics occur in the later stages of cancer and correspond to tumor cell invasiveness and metastasis (12,13). Thus, sensitive and non-destructive estimation methods for the detection of actin cytoskeleton remodeling in cancer cells are powerful tools for early diagnosis of cancer. In this regard, stiffness and other mechanical properties are potent detectable targets in cancer cytotechnology.

There are several methods to detect cell stiffness and other mechanical properties including micropipette aspiration (14), optical stretcher (15), and atomic force microscopy (AFM) (16). These technologies measure the stiffness and mechanical properties of cells in the adherent or suspended states over a wide range of physiological conditions. Micropipette aspiration and optical traps are used with suspended cells, whereas AFM is generally used for substrate-adherent cells. Despite some drawbacks such as relatively slow measurement rate and low throughput, AFM has been incrementally used to directly measure the surface stiffness of substrate-adherent cancer cells in many studies due to its certain advantages (17–21). AFM can investigate the mechanical properties of a cell surface with high sensitivity and spatial resolution under physiological cell culture conditions (22,23).

The most useful cytotechnology for detection of cancer cells, such as circulating tumor cells in the blood and biopsy for cancer, are applicable to the suspended cell state. Body fluid specimens may be the first and only pathologic specimen for clinical evaluation in metastatic cancer cases (24). Therefore, optical stretcher is one of the most useful methods to estimate whole cell stiffness in the suspended state (25), and the stiffness difference between suspended cancer and normal cells has been

* Corresponding author. Tel.: +81 6 6850 6550; fax: +81 6 6850 6557.
E-mail address: takanori.kihara@gmail.com (T. Kihara).

1389-1723/$ – see front matter
http://dx.doi.org/10.1016/j.jbiosc.2013.03.003

reported using this technique (3). Although structural differences in the actin cytoskeleton of cancer and normal cells are well understood in the adherent state (17,20), those of suspended state are unclear. Particularly, measuring the local surface stiffness of adherent cells with AFM and whole cell-body stiffness of suspended cells with optical stretcher revealed different mechanical properties (26). Therefore, to evolve the cell stiffness-based cytotechnology into a generally accepted method, it is required to characterize and compare the cell stiffness and the actin cytoskeleton structures of cancer and normal cells in both suspended and adherent states with the same experimental method.

Previously, we measured the stiffness of suspended leukocytes and trypsinized cells using AFM and a biocompatible anchor for membrane (BAM) substrate (27,28). The BAM molecule contains an oleyl group at one end that anchors the suspended cells (29). These BAM-anchored suspended cells do not move around freely like floating cells allowing us to measure their elasticity by AFM. Moreover, since BAM-anchored cells are relatively immobilized, they cannot attach to the culture substrate like adherent cells. Therefore, cell on the BAM surface are in fact anchored suspended cells and differ from both floating and adherent cells. The morphology of substrate-adherent cells varies among cells, and the orientation and distribution of their actin cytoskeleton is anisotropic and heterogeneous. On the other hand, BAM-anchored suspended cells are round and homogeneous, and exhibit an apparent isotropic actin cytoskeleton in the vicinity of their plasma membranes (30). These surface actin structures of the round cells show no apparent discrimination with respect to cell type. Although the surface actin of trypsinized and mitotic round cells appears to develop similarly, surface stiffness of the trypsinized round cells is greater than that of mitotic round cells (30). This surface stiffness is vanished by actin depolymerization. Thus, surface stiffness/elasticity measurement can detect invisible information about the maturation or strength of the actin cytoskeleton network near cell surface and may elucidate the difference in the regulatory mechanism of cell surface actin cytoskeleton.

In this study, we examined the surface stiffness of cancer and normal cells in the adherent and suspended states using AFM indentation method. Furthermore, the stiffness responses of the cancer and normal cells to actin cytoskeleton-modifying agents were determined in the adherent and suspended states.

MATERIALS AND METHODS

Materials The pyramidal probe (SN-AF01S-NT; spring constant: 0.02 N/m) was purchased from Seiko Instruments Inc. (Tokyo, Japan). Human fetal lung normal fibroblast TIG-1 cells (31), human cervical cancer HeLa cells, and human fibrosarcoma HT1080 cells, were obtained from Health Science Research Resources Bank (Osaka, Japan). Male Fisher 344 rats were purchased from Japan SLC (Shizuoka, Japan). Antibiotics were purchased from Sigma–Aldrich (St. Louis, MO, USA). BAM (Sunbright OE-020CS) was purchased from NOF Corporation (Tokyo, Japan). F-actin labeling kit was purchased from AAT Bioquest, Inc. (Sunnyvale, CA, USA). Glass based culture dishes were purchased from Asahi Glass Co., Ltd. (Tokyo, Japan). Other reagents were purchased from Sigma–Aldrich, Wako Pure Chemical Industries Ltd. (Osaka, Japan), or Life Technologies Japan Ltd. (Tokyo, Japan).

Preparation of BAM-coated dishes BAM-coated dishes were prepared as described previously (28). Briefly, polystyrene and glass based tissue culture dishes were coated with 5% BSA in PBS for 1 h. This BSA layer prevents any non-specific cell–substrate interaction. After washing with Milli-Q water, the surfaces were treated with 1 mM BAM in PBS for 30 min. Then, the BAM-coated dishes were washed and dried.

Preparation and culture of rat MSCs Rat MSCs were isolated and cultured as described previously (32). Briefly, bone marrow cells were obtained from the femoral shafts of 7-week-old male Fisher 344 rats. The cells were obtained from at least 2 rats and mixed. MEM containing 15% FBS and antibiotics (100 units/mL penicillin G, 100 μg/mL streptomycin sulfate, and 0.25 μg/mL amphotericin B) was used as the culture medium. The medium was renewed twice a week, and cells at passages 2–6 were used. The animal experiment was approved by the ethics committee of the National Institute of Advanced Industrial Science and Technology (AIST), Japan.

Cell culture and drug treatment TIG-1, HeLa, and HT1080 cells were maintained in DMEM containing 10% FBS and antibiotics. The culture medium was replaced twice a week. For adherent and suspended state examination, cells were treated with Y27632 (20 μM) or calyculin A (0.1 nM) for 12 h. For the suspended state, cells were removed from the culture dish by treating with 0.25% trypsin–0.02% EDTA in PBS and plated on a BAM-coated dish for 30 min in normal culture medium, then washed with PBS to remove unattached cells, and cultured for 12 h in drug-containing medium. Viability of the cells anchored on the BAM surface indicated more than 90% after 12 h culture (data not shown). Cells adhering to the culture dishes and BAM surfaces with or without the drug were manipulated by AFM (Fig. 1A). Actin depolymerization was induced by treating with 5 μM cytochalasin D for 2 h.

Evaluation of the actin cytoskeleton To visualize actin cytoskeleton microstructures, cultured cells in glass based dishes with or without BAM coating were fixed with 4% paraformaldehyde, permeabilized with 0.5% Triton X-100, and stained with the F-actin labeling kit. Serial sections of specimens (0.5 μm thick) were observed by confocal laser scanning microscopy (CLSM) (FV-1000; Olympus, Tokyo, Japan) using a 60× oil immersion lens (NA = 1.42). Serial images were superimposed using ImageJ software (National Institutes of Health, Bethesda, MD, USA).

AFM measurements Adherent and BAM-anchored suspended cells in medium were manipulated by AFM (Nanowizard I; JPK Instruments AG, Berlin, Germany) at room temperature. Combining the optical microscope (IX-71;

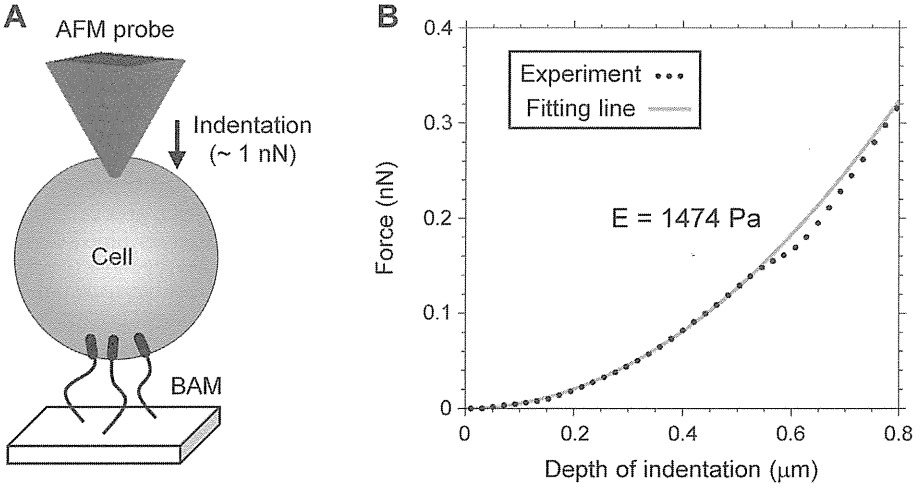

FIG. 1. AFM manipulation of BAM-anchored suspended cells. (A) Diagram of AFM indentation of suspended cells anchored to a BAM substrate. Trypsinized, detached cells were immobilized by attaching to the BAM molecules and then indented using a pyramid-shaped AFM probe. (B) A typical force–distance curve obtained from an AFM indentation experiment on an adherent HeLa cell. The black dots represent the experimental force curve line and the gray line is the Hertz model-fitting line.

Olympus) and AFM allows the probe to be positioned on a particular region of the cell surface. In this study, the AFM probe was indented the cell surface on the nuclear region with a force of up to 1 nN at 5 μm/s. The Young's modulus of the cell was calculated using the Hertz model (33). The force–distance curve for a region up to about 500 nm of cell surface indentation was fitted using JPK data processing software (JPK Instruments AG) as

$$F = \frac{E}{1-\nu^2}\frac{\tan\alpha}{\sqrt{2}}\delta^2 \quad (1)$$

where F is force, δ is depth of the probe indentation, ν is Poisson's ratio (0.5), α is half-angle to the face of the pyramidal probe (20°), and E is Young's modulus (Fig. 1B). More than 20 cells were used per experiment, and 25 points were examined on the surface of each cell. The median value was adopted as the Young's modulus of each cell (34).

Statistical analysis The changes in the Young's modulus of cells were cluster analyzed using College Analysis software created by Prof. Masayasu Fukui (Fukuyama Heisei University, Hiroshima, Japan). We used the changes in the logarithmic average of the Young's modulus for the analysis. The responsiveness of the Young's modulus to Y27632 or calyculin A treatment in the adherent or suspended states was used as the variable in each cell. The distance of each element was calculated with the standardized Euclidean distance method and the clusters were constructed using the Ward method.

RESULTS

Actin cytoskeleton structures of adherent and BAM-anchored suspended cancer and normal cells In this study, we used 2 types of normal stromal cells: rat MSCs and human TIG-1 fibroblasts, and 2 cancer cell lines: HeLa and HT1080 cells. They adhered and well spread on the normal culture substrate (Supplementary Fig. S1A). After cell detachment from the culture substrate by trypsinization and anchoring onto BAM substrate, the suspended cells showed almost similar round shape irrespective of the cell type (Supplementary Fig. S1B). Upon detachment from the normal culture substrate, the morphological anisotropy of the cells was apparently canceled.

To characterize the actin cytoskeleton structures of the adherent cell types and their reorganization during the transition from the adherent to the suspended state, F-actin was stained using fluorescein-labeled phalloidin and observed by CLSM (Fig. 2). Adherent MSCs and TIG-1 cells showed highly developed actin stress fibers across the cell body and particularly bore a clear filamentous perinuclear actin cap at their apical surface. The actin cap is an F-actin structure that forms a dome above the nucleus (35). By contrast, adherent HeLa and HT1080 cells showed weak stress fibers at the basal plane and many protrusions, fillopodia, and ruffling at the edges. They did not have any developed actin cap structures but had many short microvillus structures on their surface.

On the other hand, the F-actin structures of the examined cells changed entirely on the BAM surface. Particularly similar F-actin structures were observed irrespective of the cell type so that all BAM-anchored suspended cells had clear actin structures in the vicinity of the plasma membrane (Fig. 2). Although some spotted

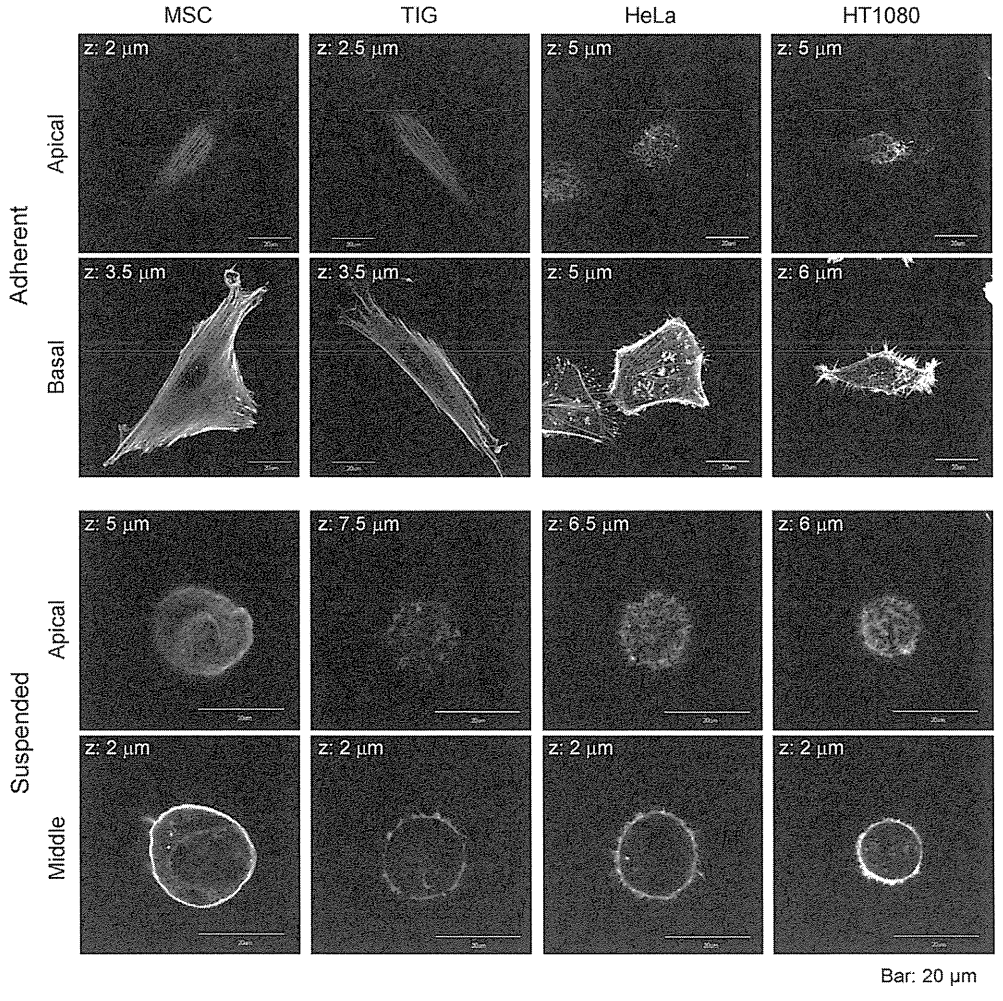

FIG. 2. CLSM images of fluorescently-labeled F-actin of cells. F-actin structures of adherent and BAM-anchored suspended cells were observed by CLSM. Superimposed images of the top, middle, and basal parts of cells are shown. The thickness of each superimposition (z) is shown in each image.

actin structures were observed inside the cells, no filamentous structures were observed. The apical actin structures of adherent and BAM-anchored suspended cancer cells were apparently similar.

Mechanical properties of adherent and BAM-anchored suspended cancer and normal cells We then determined the surface mechanical properties of the cells in the adherent and suspended states using the AFM indentation method. To reduce the effect of cell morphology, we placed the AFM probe on the nuclear region of the adherent cell surface. Fig. 3 shows the distribution of the Young's modulus of each cell type in the two adhesion states. The Young's modulus was broadly distributed irrespective of the cell type and cell adhesion states. Our previous studies revealed that the distribution of the Young's modulus of a cell follows a log-normal pattern (28,34). Therefore, we have shown the logarithmic average of the Young's modulus for each condition.

The distribution of the Young's moduli of adherent normal stromal cells was clearly higher than those of cancer cells (Fig. 3). Upon detachment from the substrate and alteration in actin cytoskeleton and cell morphology, the distribution of the Young's modulus of normal stromal cells decreased but that of cancer cells was relatively unchanged. Even in the suspended state, the elastic values of normal stromal cells remained higher than those of cancer cells.

The Young's moduli of adherent and BAM-anchored suspended cells were notably diminished by actin depolymerization with cytochalasin D (Supplementary Fig. S2) indicating the significant contribution of the cell surface actin filaments to the observed mechanical properties.

Mechanical responsiveness of cancer and normal cells to perturbations of the actin cytoskeleton To evaluate the contribution of F-actin structures to the mechanical properties, we examined the responsiveness of the mechanical properties of the cells to actin cytoskeleton-modifying agents, Y27632 and calyculin A. Y27632 is a ROCK inhibitor that prevents and attenuates stress fiber formation (36). On the other hand, calyculin A is a myosin light chain phosphatase inhibitor that activates actomyosin formation and enhances actin polymerization (37).

Addition of Y27632 to the cultured cells reduced the distribution of the Young's modulus in all the cell types and adhesion states (Fig. 4). Particularly, the Young's moduli of normal stromal cells significantly decreased both in the adherent and suspended states. On the other hand, the reduction rates of the Young's moduli of cancer cells after treatment with Y27632 were lower and almost the same in the adherent and suspended states. After Y27632 treatment, the distribution of the Young's moduli of BAM-anchored suspended normal stromal cells became almost the same as that of BAM-anchored suspended cancer cells.

In normal stromal cells treated with calyculin A, the distributions of the Young's modulus were almost unchanged in the adherent and suspended states (Fig. 4). On the other hand, in cancer cells, the distributions of the Young's modulus were slightly increased by calyculin A treatment in both the adherent and suspended states.

Finally, we performed statistical data analysis on the mechanical responsiveness trends of the cells. The changes in the logarithmic average of the Young's modulus in response to Y27632 and calyculin A in the adherent or suspended state were used as variables in each cell type. Fig. 5A shows dendrogram of the cluster analysis in which normal stromal and cancer cells belong to distinct clusters. The responsiveness characteristics of normal stromal and cancer cells to Y27632 and calyculin A treatment in the adherent and suspended states are shown in Fig. 5B. The square value of each responsiveness for the agents was used for this purpose. Normal stromal cells were strongly affected by only Y27632 in the adherent and suspended states. On the other hand, cancer cells were equally affected by calyculin A and Y27632. The responsiveness to actin-modifying agents was almost unchanged in the adherent and suspended states for both normal stromal and cancer cells. Therefore, the regulatory mechanisms for F-actin structures are different in normal stromal and cancer cells regardless of their adhesion states.

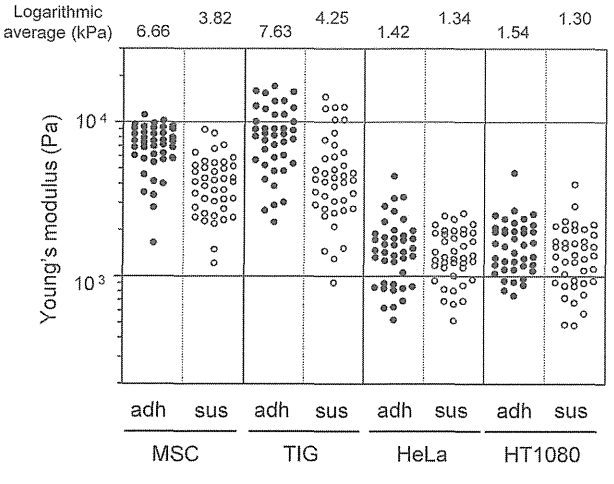

FIG. 3. Young's modulus of cells in the adherent and suspended states. The distribution and logarithmic average of the Young's moduli of the 4 cell types in adhesion (closed circles) *vs.* suspension states (open circles) are shown. Each condition shows the Young's modulus of 40 independent cells.

DISCUSSION

This study presented an overview of the surface mechanics and actin cytoskeleton architecture of normal stromal and cancer cells in the adherent and suspended states. Adherent normal stromal cells formed highly organized actin cap and exhibited high stiffness at their apical surface, whereas adherent cancer cells lacked the actin cap and showed lower stiffness relative to the normal cells (Figs. 2 and 3). The actin cap is an F-actin structure that forms a dome above the nucleus, tightly regulating the shape of the nucleus in adherent fibroblasts (35). Furthermore the actin cap regulates surface stiffness and thickness of adherent rat MSCs; a developed actin cap increases surface stiffness (34). Thus, it is easily conceivable that the observed difference in the mechanical properties of adherent normal stromal and cancer cells reflects the completely different F-actin structures at the apical surface of these cell types. This finding is also consistent with the previous studies (4,17). On the other hand, detachment from the substrate and reorganization of F-actin structures into cortical actin in the vicinity of the plasma membrane, made it difficult to define a difference between actin structures of BAM-anchored suspended cancer and normal cells (Fig. 2). Nevertheless, the distribution of the Young's modulus of BAM-anchored suspended normal stromal cells remained higher than that of cancer cells (Fig. 3). We previously showed that surface stiffness of the trypsinized round cells was greater than that of mitotic round cells, although they had similar actin structures (30). Furthermore, the elastic responsiveness of normal stromal and cancer cells to the actin-modifying agents Y27632 and calyculin A were distinct in the suspended state (Figs. 4 and 5). Therefore, the surface stiffness can provide the invisible information about the states and structures of the actin cytoskeleton on the cell surface. Together, these results define a key distinction between mechanical and actin cytoskeleton features of cancer and normal stromal cells.

The need for reliable biomarkers for cancer detection and analysis is critical due to complexity of the disease. Mechanical properties such as elasticity and viscosity are markers independent

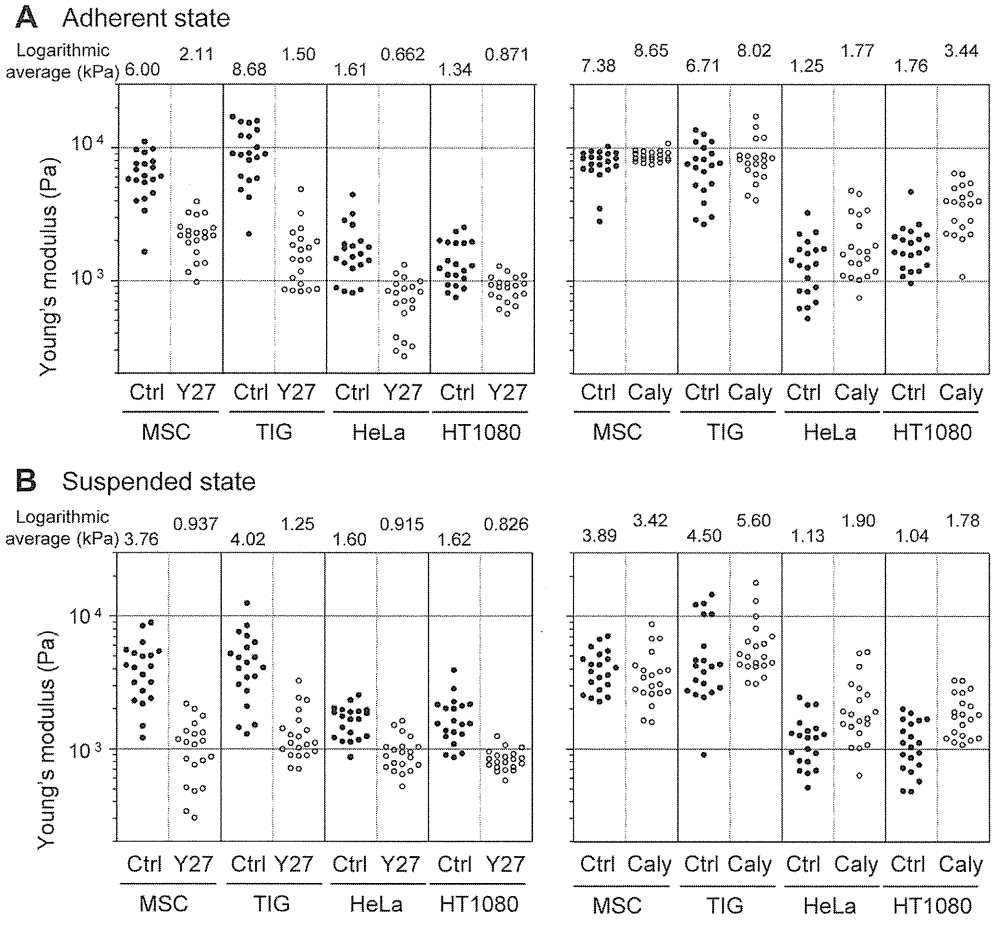

FIG. 4. Elastic responses of adherent and BAM-anchored suspended cells following treatment with Y27632 and calyculin A. The distribution and logarithmic average of the Young's moduli of the cell types in adhesion (A) and suspension (B) states are shown. Left graphs show the results of treatment with 20 μM Y27632 (Y27) and the right graphs are those of treatment with 0.1 nM calyculin A (Caly). Each condition shows the Young's modulus of 20 independent cells.

from the commonly used biochemical markers of cancer cells. Development of reliable methods for measuring the mechanical properties of various cell types would contribute to early cancer screening. In this study, we suggested the capability of the discrimination between cancer and normal cells in both the adherent and suspended states using cell surface stiffness. The whole-cell deformability of cancer and normal cells in the suspended state are also different, and metastatic cancer cells are easily deformed by optical stretching (3,38). Therefore, the deformability of both local-surface and whole-body of suspended

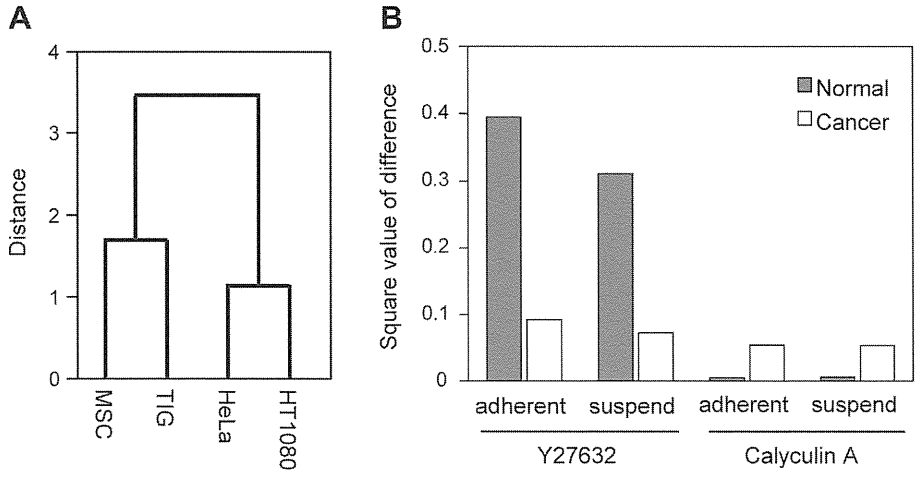

FIG. 5. Statistical analysis of the responsiveness of the Young's moduli of drug-treated adherent and BAM-anchored suspended cells. (A) Dendrogram showing the cluster analysis of cells using the responsiveness to actin cytoskeleton-modifying agents in the adherent and suspended states. The responsiveness of the Young's modulus to Y27632 and calyculin A in the adherent or suspended states was used as variables for each cell type. (B) The elastic response behaviors of adherent and BAM-anchored suspended cells after treatment with Y27632 and calyculin A. The square values of the logarithmic average difference of the Young's modulus in the non-treated control condition from the agent-treated condition were used.

cancer cells are higher than normal cells. The easy deformability of cancer cells could be due to their unique regulatory mechanisms for actin cytoskeleton, which controls the mechanical properties of cancer cells. Recently, high-speed measuring method for cell deformation throughout the narrow microchannel has been developing (39). The measuring rate has reached more than 1000 cells/s. For the future, the precise and high-speed measurement of the mechanical properties or deformability of suspended cells can be employed for cancer cytotechnology.

Supplementary data related to this article can be found at http://dx.doi.org/10.1016/j.jbiosc.2013.03.003.

ACKNOWLEDGMENTS

We thank Prof. Masayasu Fukui (Fukuyama Heisei University, Hiroshima, Japan) for permission to use his statistical analysis software, College Analysis. This work was supported by a Grant-in-Aid for Scientific Research on Innovative Areas "Nanomedicine Molecular Science" (No. 2306) from the Ministry of Education, Culture, Sports, Science and Technology of Japan to T.K. and J.M., and a grant for a research project on industrialization of medical innovation and technology from Okinawa Prefecture, Japan to J.M.

References

1. **Eiraku, M., Takata, N., Ishibashi, H., Kawada, M., Sakakura, E., Okuda, S., Sekiguchi, K., Adachi, T., and Sasai, Y.:** Self-organizing optic-cup morphogenesis in three-dimensional culture, Nature, **472**, 51–56 (2011).
2. **Suresh, S., Spatz, J., Mills, J. P., Micoulet, A., Dao, M., Lim, C. T., Beil, M., and Seufferlein, T.:** Connections between single-cell biomechanics and human disease states: gastrointestinal cancer and malaria, Acta Biomater., **1**, 15–30 (2005).
3. **Guck, J., Schinkinger, S., Lincoln, B., Wottawah, F., Ebert, S., Romeyke, M., Lenz, D., Erickson, H. M., Ananthakrishnan, R., Mitchell, D., and other 3 authors:** Optical deformability as an inherent cell marker for testing malignant transformation and metastatic competence, Biophys. J., **88**, 3689–3698 (2005).
4. **Cross, S. E., Jin, Y. S., Rao, J., and Gimzewski, J. K.:** Nanomechanical analysis of cells from cancer patients, Nat. Nanotechnol., **2**, 780–783 (2007).
5. **Dai, J. and Sheetz, M. P.:** Mechanical properties of neuronal growth cone membranes studied by tether formation with laser optical tweezers, Biophys. J., **68**, 988–996 (1995).
6. **Trickey, W. R., Vail, T. P., and Guilak, F.:** The role of the cytoskeleton in the viscoelastic properties of human articular chondrocytes, J. Orthop. Res., **22**, 131–139 (2004).
7. **Sugitate, T., Kihara, T., Liu, X.-Y., and Miyake, J.:** Mechanical role of the nucleus in a cell in terms of elastic modulus, Curr. Appl. Phys., **9**, e291–e293 (2009).
8. **Pelling, A. E., Dawson, D. W., Carreon, D. M., Christiansen, J. J., Shen, R. R., Teitell, M. A., and Gimzewski, J. K.:** Distinct contributions of microtubule subtypes to cell membrane shape and stability, Nanomedicine, **3**, 43–52 (2007).
9. **Nishimura, S., Nagai, S., Katoh, M., Yamashita, H., Saeki, Y., Okada, J., Hisada, T., Nagai, R., and Sugiura, S.:** Microtubules modulate the stiffness of cardiomyocytes against shear stress, Circ. Res., **98**, 81–87 (2006).
10. **Rao, J. Y., Hurst, R. E., Bales, W. D., Jones, P. L., Bass, R. A., Archer, L. T., Bell, P. B., and Hemstreet, G. P., 3rd:** Cellular F-actin levels as a marker for cellular transformation: relationship to cell division and differentiation, Cancer Res., **50**, 2215–2220 (1990).
11. **Hemstreet, G. P., 3rd, Rao, J. Y., Hurst, R. E., Bonner, R. B., Jones, P. L., Vaidya, A. M., Fradet, Y., Moon, R. C., and Kelloff, G. J.:** Intermediate endpoint biomarkers for chemoprevention, J. Cell. Biochem. Suppl., **16I**, 93–110 (1992).
12. **Rao, J.:** Targeting actin remodeling profiles for the detection and management of urothelial cancers – a perspective for bladder cancer research, Front. Biosci., **7**, e1–e8 (2002).
13. **Lu, Q. Y., Jin, Y. S., Pantuck, A., Zhang, Z. F., Heber, D., Belldegrun, A., Brooks, M., Figlin, R., and Rao, J.:** Green tea extract modulates actin remodeling via Rho activity in an in vitro multistep carcinogenic model, Clin. Cancer Res., **11**, 1675–1683 (2005).
14. **Evans, E. and Yeung, A.:** Apparent viscosity and cortical tension of blood granulocytes determined by micropipet aspiration, Biophys. J., **56**, 151–160 (1989).
15. **Guck, J., Ananthakrishnan, R., Moon, T. J., Cunningham, C. C., and Kas, J.:** Optical deformability of soft biological dielectrics, Phys. Rev. Lett., **84**, 5451–5454 (2000).
16. **Radmacher, M., Fritz, M., Kacher, C. M., Cleveland, J. P., and Hansma, P. K.:** Measuring the viscoelastic properties of human platelets with the atomic force microscope, Biophys. J., **70**, 556–567 (1996).
17. **Li, Q. S., Lee, G. Y., Ong, C. N., and Lim, C. T.:** AFM indentation study of breast cancer cells, Biochem. Biophys. Res. Commun., **374**, 609–613 (2008).
18. **Faria, E. C., Ma, N., Gazi, E., Gardner, P., Brown, M., Clarke, N. W., and Snook, R. D.:** Measurement of elastic properties of prostate cancer cells using AFM, Analyst, **133**, 1498–1500 (2008).
19. **Fuhrmann, A., Staunton, J. R., Nandakumar, V., Banyai, N., Davies, P. C., and Ros, R.:** AFM stiffness nanotomography of normal, metaplastic and dysplastic human esophageal cells, Phys. Biol., **8**, 015007 (2011).
20. **Cross, S. E., Jin, Y. S., Lu, Q. Y., Rao, J., and Gimzewski, J. K.:** Green tea extract selectively targets nanomechanics of live metastatic cancer cells, Nanotechnology, **22**, 215101 (2011).
21. **Lekka, M., Pogoda, K., Gostek, J., Klymenko, O., Prauzner-Bechcicki, S., Wiltowska-Zuber, J., Jaczewska, J., Lekki, J., and Stachura, Z.:** Cancer cell recognition – mechanical phenotype, Micron, **43**, 1259–1266 (2012).
22. **Collinsworth, A. M., Zhang, S., Kraus, W. E., and Truskey, G. A.:** Apparent elastic modulus and hysteresis of skeletal muscle cells throughout differentiation, Am. J. Physiol. Cell. Physiol., **283**, C1219–C1227 (2002).
23. **Costa, K. D.:** Imaging and probing cell mechanical properties with the atomic force microscope, Methods Mol. Biol., **319**, 331–361 (2006).
24. **Stancel, G. A., Coffey, D., Alvarez, K., Halks-Miller, M., Lal, A., Mody, D., Koen, T., Fairley, T., and Monzon, F. A.:** Identification of tissue of origin in body fluid specimens using a gene expression microarray assay, Cancer Cytopathol., **120**, 62–70 (2012).
25. **Guck, J., Ananthakrishnan, R., Mahmood, H., Moon, T. J., Cunningham, C. C., and Kas, J.:** The optical stretcher: a novel laser tool to micromanipulate cells, Biophys. J., **81**, 767–784 (2001).
26. **Maloney, J. M., Nikova, D., Lautenschlager, F., Clarke, E., Langer, R., Guck, J., and Van Vliet, K. J.:** Mesenchymal stem cell mechanics from the attached to the suspended state, Biophys. J., **99**, 2479–2487 (2010).
27. **Kagiwada, H., Nakamura, C., Kihara, T., Kamiishi, H., Kawano, K., Nakamura, N., and Miyake, J.:** The mechanical properties of a cell, as determined by its actin cytoskeleton, are important for nanoneedle insertion into a living cell, Cytoskeleton (Hoboken), **67**, 496–503 (2010).
28. **Shimizu, Y., Kihara, T., Haghparast, S. M., Yuba, S., and Miyake, J.:** Simple display system of mechanical properties of cells and their dispersion, PLoS One, **7**, e34305 (2012).
29. **Kato, K., Umezawa, K., Funeriu, D. P., Miyake, M., Miyake, J., and Nagamune, T.:** Immobilized culture of nonadherent cells on an oleyl poly(ethylene glycol) ether-modified surface, Biotechniques, **35**, 1014–1021 (2003).
30. **Shimizu, Y., Haghparast, S. M., Kihara, T., and Miyake, J.:** Cortical rigidity of round cells in mitotic phase and suspended state, Micron, **43**, 1246–1251 (2012).
31. **Ohashi, M., Aizawa, S., Ooka, H., Ohsawa, T., Kaji, K., Kondo, H., Kobayashi, T., Noumura, T., Matsuo, M., Mitsui, Y., and other 5 authors:** A new human diploid cell strain, TIG-1, for the research on cellular aging, Exp. Gerontol., **15**, 121–133 (1980).
32. **Kihara, T., Hirose, M., Oshima, A., and Ohgushi, H.:** Exogenous type I collagen facilitates osteogenic differentiation and acts as a substrate for mineralization of rat marrow mesenchymal stem cells in vitro, Biochem. Biophys. Res. Commun., **341**, 1029–1035 (2006).
33. **Hertz, H.:** Über die Berührung fester elastischer Körper, J. Reine Angew. Math., **92**, 156–171 (1881).
34. **Kihara, T., Haghparast, S. M., Shimizu, Y., Yuba, S., and Miyake, J.:** Physical properties of mesenchymal stem cells are coordinated by the perinuclear actin cap, Biochem. Biophys. Res. Commun., **409**, 1–6 (2011).
35. **Khatau, S. B., Hale, C. M., Stewart-Hutchinson, P. J., Patel, M. S., Stewart, C. L., Searson, P. C., Hodzic, D., and Wirtz, D.:** A perinuclear actin cap regulates nuclear shape, Proc. Natl. Acad. Sci. USA, **106**, 19017–19022 (2009).
36. **Uehata, M., Ishizaki, T., Satoh, H., Ono, T., Kawahara, T., Morishita, T., Tamakawa, H., Yamagami, K., Inui, J., Maekawa, M., and Narumiya, S.:** Calcium sensitization of smooth muscle mediated by a Rho-associated protein kinase in hypertension, Nature, **389**, 990–994 (1997).
37. **Ishihara, H., Ozaki, H., Sato, K., Hori, M., Karaki, H., Watabe, S., Kato, Y., Fusetani, N., Hashimoto, K., and Uemura, D.:** Calcium-independent activation of contractile apparatus in smooth muscle by calyculin-A, J. Pharmacol. Exp. Ther., **250**, 388–396 (1989).
38. **Lincoln, B., Erickson, H. M., Schinkinger, S., Wottawah, F., Mitchell, D., Ulvick, S., Bilby, C., and Guck, J.:** Deformability-based flow cytometry, Cytometry A, **59**, 203–209 (2004).
39. **Hirose, Y., Tadakuma, K., Higashimori, M., Arai, T., Kaneko, M., Iitsuka, R., Yamanishi, Y., Arai, F.:** A new stiffness evaluation toward high speed cell sorter, pp. 4113–4118, in: Proceedings of 2010 IEEE International Conference on Robotics and Automation. IEEE (2010).

Society For Biomaterials

Evaluation of the capacity of mosaic-like porous ceramics with designed pores to support osteoconduction

Kay Teraoka,[1*] Tomotaka Kato,[2*] Koji Hattori,[3] Hajime Ohgushi[4]

[1]Advanced Manufacturing Research Institute, National Institute of Advanced Industrial Science and Technology, Aichi, Japan
[2]Department of Periodontology, Nippon Dental University, Tokyo, Japan
[3]Faculty of Nursing and Rehabilitation, Konan Women's University, Hyogo, Japan
[4]Health Research Institute, National Institute of Advanced Industrial Science and Technology, Hyogo, Japan

Received 1 October 2012; revised 11 December 2012; accepted 6 February 2013
Published online 9 May 2013 in Wiley Online Library (wileyonlinelibrary.com). DOI: 10.1002/jbm.a.34663

Abstract: Under osteoconductive conditions, porous calcium phosphate ceramics are known to induce new bone formation within their pores. A critical aspect of the design of porous ceramics is the geometrical features of their pores, with regard to promoting bone formation and mass transfer management in pore networks. However, the pore geometries of common porous ceramics lack clear details. Further, the connections between pores are hard to characterize and thus have not been thoroughly researched. To address these issues, we have developed an original method for fabricating porous ceramics, which we have termed "mosaic-like ceramics fabrication (MLCF)." Using MLCF, pore geometries can be designed and fabricated by each unit, and a network covering all the pores can be fabricated. Furthermore, MLCF can be used to build porous ceramics with custom-made shapes. In this study, we assessed the osteogenic influences of MLCF products (MLPC) composed of hydroxyapatite units on the differentiation of rat bone-marrow-derived mesenchymal stem cells (MSCs) *in vitro* and *in vivo*. Two types of commercial porous artificial bone were used as positive controls. MLPC was superior in osteogenic potential, and proved to be a reliable scaffold for bone tissue engineering. Furthermore, this study succeeded in defining the important geometries for osteoconduction. © 2013 Wiley Periodicals, Inc. J Biomed Mater Res Part A: 101A: 3571–3579, 2013.

Key Words: ceramic scaffold, pore geometries, osteoconductivity, mesenchymal stem cells, bone tissue engineering

How to cite this article: Teraoka K, Kato T, Hattori K, Ohgushi H. 2013. Evaluation of the capacity of mosaic-like porous ceramics with designed pores to support osteoconduction. J Biomed Mater Res Part A 2013:101A:3571–3579.

INTRODUCTION

Synthetic calcium phosphates, such as hydroxyapatite (HA), have been widely used as an artificial bone material owing to their biocompatibility.[1,2] The artificial bones are usually polycrystalline and are available in versatile forms, such as blocks, granules, and paste. Most of them fulfill their bone repair duty with the aid of the physiological activities of bone tissue.

A simple strategy to take advantage of the natural physiological processes involved in bone repair is to use porous calcium phosphate ceramics. There are many methods available for making macroporous ceramics, with each method producing its own characteristic pore shapes. One method used for macroporous ceramic fabrication is the replica method.[3] The replica method essentially makes pores based on templates with a cellular structure. There are many synthetic and natural templates, but in the case of porous HA production, coral is one of the most well-known natural templates.[4,5]

A common method for fabricating porous ceramics, the sacrificial template method, consists of compaction and sintering of ceramic powder or slurry with sacrificial phases.[3] The sacrificial phases are commonly polymeric or carbon, and leave pores resembling their shapes after sintering. The direct foaming method is another popular fabrication technique for porous ceramics.[6,7] This method helps in the creation of pores, as bubbles are generated when gas is blown into the HA slurry. These bubbles within the slurry are fixed by solidifying the slurry, resulting in pores with bubble-like spherical shapes and narrow interconnections at the contact points between the bubbles. Usually, the set HA slurry has to be sintered to be strengthened.

Although pore shapes are dependent on the manufacturing process, Hulbert et al.[8] concluded that porous ceramics showed the ability to accept substantial bone ingrowth when their pore size was greater than 100 μm. Karageorgiou et al.[9] confirmed that better osteogenesis occurs for implants with pores >300 μm. Furthermore, Kuhne et al. showed that coralline porous HA ceramics with an average pore size of 260 μm effectively facilitated bone ingrowth.[10] Consequently, pore sizes of a few hundred microns have

*These authors contributed equally to this work.
Correspondence to: K. Teraoka; e-mail: ok-teraoka@aist.go.jp

been used as a standard for promoting new bone formation. There are currently several calcium phosphate ceramics on the market with pores in this size range.

However, the "pore size" of common porous ceramics is indeterminate in a precise sense because the pores exhibit various shapes, and pore sizes are measuring-direction-sensitive. This is a critical problem with regard to determining how the pore shape (cause) affects osteoconduction (effect). Optimal pore geometries for bone formation could be analytically extracted from pores with definable shapes that achieve successful bone formation. Porous ceramics with definable pore shapes are essential to address this issue, but commonly there is little control over pore geometries.

Another important research issue relating to porous ceramics is management of mass transfer in the pore networks. Generally, the pore network consists of pores and inter-pore paths and the paths are narrower than the pores. Therefore, the paths are the limiting factor for transfer, thereby requiring an efficient design that allows for the infiltration of viscous fluid containing cells into each pore of porous ceramics. These paths also need to be amenable to bone formation but, at the same time, are required to maintain adequate mass transfer until bone repair is complete. Accordingly, the pore network requires a robust design that supports both long-lasting mass transfer and bone formation. Currently, however, path geometries are not easy to control or well characterized, and there is no convincing evidence relating to the connectivity of the pores in whole ceramic bodies.

To address the above-mentioned issues, we developed an original method for fabricating porous ceramics, which we have termed "mosaic-like ceramics fabrication" (MLCF). MLCF fabricates porous ceramics as an assembly of small functional units made of biomaterials (Fig. 1). By employing MLCF, pore geometries can be designed and fabricated at the unit level. These precisely designed pores can be evenly distributed throughout the assembly, and the number of pores is always in multiples of the number of units used. Importantly, isolated pores are not created in the assembly process, rather inter-unit gaps are created; hence, MLCF can deductively guarantee complete inter-connectivity of pores. Furthermore, MLCF can be used to build custom-made shapes. MLCF products are called "mosaic-like porous ceramics (MLPC)." MLPCs have been prototyped using common biomaterials.[11,12] In this study, we assessed the influence of MLPCs on the differentiation and osteogenesis of rat bone marrow-derived mesenchymal stem cells (MSCs) *in vitro* and *in vivo*. Two types of commercial porous artificial bone were used as positive controls.

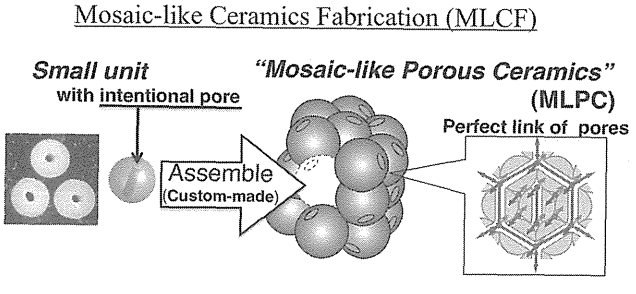

FIGURE 1. Basic concept of mosaic-like ceramics fabrication (MLCF). [Color figure can be viewed in the online issue, which is available at wileyonlinelibrary.com.]

MATERIALS AND METHODS

Preparation of MLPC

MLPCs were fabricated by assembling HA units into a disk shape (Fig. 2, left). As the factor of interest was pore geometry, we selected HA to minimize the influence of dissolution. The size of the disk was based on that of comparable porous HA disks (5 mm in diameter and 2 mm in height), and was achievable because of the customizable capabilities of MLCF.

The HA unit was designed to have a ϕ1 mm spherical shape with a cylindrical through-hole as the osteoconductive pore. The through-hole was fabricated along with the central axis of the HA unit, and the through-hole's diameter was determined to be 226 μm, in accordance with the valid diameter for cell recruitment.[13]

Each HA unit was prepared by dropping HA slurry into a calcium chloride solution (coagulant) and subsequent sintering. HA slurry was prepared by mixing HA powder (HAP 100, Taihei Chem. Ind. Co., Ltd., Japan) with a sodium alginate solution. The HA powder was pulverized for 30 min before slurry preparation by using a pulverisette ball mill (Fritsch Japan Co., Ltd) with a silicon nitride pod (500 mL) and ϕ10 mm media (total weight: 202 g). The HA slurry was dropped quantitatively into the calcium chloride solution to form HA spheres. One through-hole of ϕ226 μm was formed for each HA sphere before sintering using a split mold with pitting needles.

The assembly of the MLPC was performed by packing HA units into a cylindrical plastic mold in three layers such that the layers formed a hexagonal closest-packing arrangement. Some packing irregularities existed in the MLPC because of the mold size, which resulted in some irregular gaps between the units. This kept the porosity around 47%, while ideal hexagonal closest packing exhibits 26%. The assemblies were fixed by a sintering process.

For comparison, we purchased two commercially available synthetic porous HA ceramics of 5 mm in diameter and 2 mm in height (abbreviated as HA-A and HA-B). Both ceramics have been widely used in orthopedic, craniofacial, and dental fields. HA-A, shown in Figure 2 (center), has

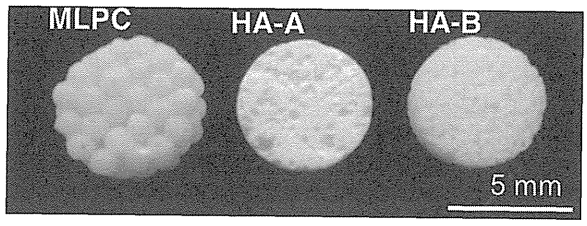

FIGURE 2. Overview images of the MLPC (left), HA-A (middle) and HA-B (right). [Color figure can be viewed in the online issue, which is available at wileyonlinelibrary.com.]

pores ranging from 0.1 to 500 μm in diameter and 50% porosity.[14] HA-B, shown in Figure 2 (right), has pores ranging from 50 to 300 μm in diameter and 75% porosity.[15,16]

Rat bone-marrow-derived MSC preparation and culture

All procedures used in animal experiments conformed to the Guidelines for the Care and Use of Laboratory Animals of the National Institute of Advanced Industrial Science and Technology of Japan. Rat bone-marrow-derived stromal cells (BMSCs) were obtained from the femoral shafts of 7-week-old Fischer 344 male rats (Japan SLC, Shizuoka, Japan), as described previously.[17] Both ends of the femur were cut away from the epiphysis, and the bone marrow was flushed out using 10 mL of culture medium injected through a 21-gauge syringe needle. The released marrow cells were collected in a T-75 flask (Costar, MA, USA) and maintained in a humidified 5% CO_2 balanced-air incubator at 37°C. The culture medium consisted of Eagle's minimal essential medium (EMEM; Nacalai, Kyoto, Japan) containing 15% fetal bovine serum (JRH Bioscience, KS, USA) and 1% antibiotics (100 U/mL penicillin G, 100 μg/mL streptomycin sulfate, and 0.25 μg/mL amphotericin B, Sigma-Aldrich, MO, USA). The medium was changed three times a week. The adherent cells were regarded as BMSCs. After 7 days of primary culture, BMSCs were then detached from the flasks using trypsin/EDTA (0.05% trypsin, 0.53 m*M* EDTA-4Na, Invitrogen, CA, USA), concentrated by centrifugation at 400× *g* for 5 min at room temperature and resuspended at a density of 10^6 cells/mL in a 12-mL tube with EMEM. The three different HA ceramic disks were placed in the 12-mL tube and soaked in 1 mL of cell suspension, following which a partial vacuum was applied, in accordance with the methods used in a previous study.[18] After 30 min, the disks were rinsed twice with PBS and moved to 24-well tissue culture plates (BD Biosciences, CA, USA). Each disk was subcultured in 1 mL of osteogenic media. The osteogenic media consisted of culture medium supplemented with 10 m*M* β-glycerophosphate (Calbiochem, CA, USA), 0.28 m*M* ascorbic acid-2-phosphate (Wako Pure Chemical Industries, Osaka, Japan) and 10 n*M* dexamethasone (Nacalai Tesque, Kyoto, Japan). The medium was changed three times a week and the disks were maintained for 2 weeks. This study consisted of three groups of HA ceramic disks as follows: BMSCs cultured on MLPC (BMSCs/MLPC), on HA-A (BMSCs/HA-A), or on HA-B (BMSCs/HA-B). The osteoconductive properties of the disks were then analyzed *in vivo* and *in vitro*.

Alkaline phosphatase staining

Alkaline phosphatase (ALP) staining was performed as previously described.[19,20] The cultured disks were rinsed twice with PBS and fixed with 10% natural-buffered formaldehyde for 10 min at 4°C. The fixed disks were soaked in 0.1% naphthol AS-MX phosphate and 0.1% fast red violet LB salt in 56 m*M* 2-amino-2-methyl-1,3-propanediol (pH 9.9) for 10 min at room temperature, washed with PBS, and observed using an objective microscope (MZ FLIII; Leica Co., Tokyo, Japan). Using a cryostat (CM1850; Leica Microsystems), the disks were cut through the central portion to facilitate a sagittal sectional view.

Biochemical analyses *in vitro*

ALP activity and osteocalcin secretion from the cultured disks were assessed *in vitro*. For the measurement of ALP activity, the disks were washed twice with PBS, crushed, and homogenized in 500 μL of 0.2% Nonidet P-40 supplemented with 1 m*M* $MgCl_2$ and 50 m*M* Tris–HCl buffer. After homogenization, they were centrifuged at 400× *g* for 5 min at 4°C. The supernatants were then assayed for ALP activity. ALP activity was quantified as μ*M* of *p*-nitrophenol released per disk for 1 min at 37°C.

Osteocalcin was measured in accordance with the modified method previously reported.[21] After 13 days of subculture, the disks were transferred into new 24-well culture plates with 1 mL of fresh osteogenic medium. The disks were incubated for 24 h at 37°C and the culture medium was prepared for analysis of osteocalcin using an enzyme-linked immunosorbent assay (Rat osteocalcin ELISA kit DS; DS Pharma Biomedical, Japan).

Subcutaneous implantation

After subculture of BMSCs on disks using the above method, the cultured disks were subcutaneously implanted into the backs of rats. Syngeneic Fischer 344 rats were anesthetized with intraperitoneal injections of pentobarbital (Nembutal; Dainippon Pharmaceutical, Tokyo, Japan) at a dose of 35 mg/kg body weight. The cultured disks were implanted subcutaneously into the back of the recipient rats (total four recipients) at six different sites. The disks (total 23 disks) were harvested 6 weeks after implantation.

Micro-focus computed tomography

New bone formation in the disks was observed by micro-focus computed tomography (μCT; MCT-CB 130 MF, Shimadzu, Japan). Each disk was scanned at a voltage of 100 kV, 100 μA, and a pixel size of 6.86 μm. Newly formed bone inside the ceramics was identified by assessing the voxel intensity of the μCT images. In cases where new bone formation is substantial, voxel intensity histograms exhibit three peaks. A peak representing new bone will appear between two other peaks: the higher peak representing ceramics, and the lower peak representing soft tissue. Voxel intensity histograms were derived from the cubic region of interest (ROI) at the central portion of the disks. Once all disks were scanned, one disk was used for histological analysis and remaining disks were used for biochemical analyses.

Histological analysis

After micro CT analysis, the disks were fixed in 10% neutral buffered formalin solution overnight and decalcified with K-CX solution (Falma Co., Tokyo, Japan). After dehydration via a graded series of ethanol concentrations, the disks were embedded in paraffin and cut into 6-μm sections at the center of each specimen, following a plane perpendicular to the round surface of the disks. The sections were

stained with hematoxylin and eosin and examined using an optical microscope.

Biochemical analysis *in vivo*

Osteocalcin content analysis of the disks was performed according to the modified method described in our previous report.[22] Briefly, each disk was crushed, homogenized in 500 μL of 0.2% Nonidet P-40 supplemented with 1 m*M* $MgCl_2$ and 50 m*M* Tris-HCl buffer, and centrifuged at 400× *g* for 15 min at 4°C. Osteocalcin from the disks was extracted from the sediment of the Nonidet P-40 extract with 5 mL of 20% formic acid for 2 weeks at 4°C. An aliquot of the formic acid extract was applied to a pre-packed Sephadex G-25 column (NAP-25 column; Amersham Pharmacia Biotech AB, Uppsala, Sweden) and eluted with 1 mL of 10% formic acid. The protein fractions were pooled, lyophilized, and subjected to enzyme-linked immunosorbent assay (Rat osteocalcin ELISA kit DS; DS Pharma Biomedical) for rat osteocalcin.

Statistical analysis

Statistical analyses were performed using the statistical software ystat2008 (Igakutosho-shuppan Ltd., Japan). ALP activity and osteocalcin content were analyzed using one-way analysis of variance (ANOVA). Significances of individual differences were evaluated by using Bonferroni correction. In all analyses, the significance level was set at $P < 0.05$.

RESULTS

ALP staining *in vitro*

Figure 3 shows the ALP staining of the cross-section of three disks. All the three disk groups were stained on the surface of the disks. In both BMSCs/HA-A [Fig. 3(B,E)] and BMSCs/HA-B [Fig. 3(C,F)], the insides of the disks stained lightly with ALP; however, in the BMSCs/MLPC group, ALP staining was also evident within the gaps and through-holes [(Fig. 3(A D)]. In addition, ALP staining penetrated much deeper in this group than in the other groups. This finding shows that BMSCs adhered more deeply within the pores and that the MLPC had increased osteogenic ability.

Biochemical analysis *in vitro*

We previously reported that *in vitro* osteogenic differentiation can occur on the surface of many different ceramics.[20] As a result of these findings, we examined whether interconnected porous calcium HA ceramics can support *in vitro* differentiation by measuring ALP activity. In addition, osteocalcin secretion was also reported *in vitro* for osteogenic differentiation.[21] To quantify the osteogenic potential of cultured composites consisting of BMSCs and HA ceramics, biochemical parameters such as ALP activity and osteocalcin secretion were measured 2 weeks after subculture. The mean ALP activities per 10 min/disk were 3.10 μmol for BMSCs/MLPC, 2.31 μmol for BMSCs/HA-A, and 2.92 μmol for BMSCs/HA-B. The mean ALP activity of the BMSCs/MLPC group was highest among the three groups tested [(Fig. 4(A)]. Significant differences in the ALP activity were found between the BMSCs/MLPC and BMSCs/HA-A groups ($p < 0.05$). The mean osteocalcin content was 16.10 μg/mL in BMSCs/MLPC, 7.55 μg/mL in BMSCs/HA-A, and 9.49 μg/mL in BMSCs/HA-B [(Fig. 4(B)]. Significant differences in the osteocalcin content were found between the BMSCs/MLPC and BMSCs/HA-A groups ($p < 0.01$), and the BMSCs/MLPC and BMSCs/HA-B groups ($p < 0.01$).

Microcomputed tomography analysis *in vivo*

Figure 5(A–C) shows μCT images of the disks before the *in vivo* test (A: MLPC, B: HA-A, and C: HA-B). All the images comprise images of ceramics and empty pores. Voxel intensity histograms of MLPC and HA-A exhibited definite bimodal peak profiles: a lower peak attributable to empty pores and a higher peak attributable to ceramics. In the case of HA-B, the voxel intensity histograms showed a lower peak and an ambiguous plateau in the middle- and high-intensity ranges. The plateau was formed because of high porosity of HA-B; high porosity increases the rate of

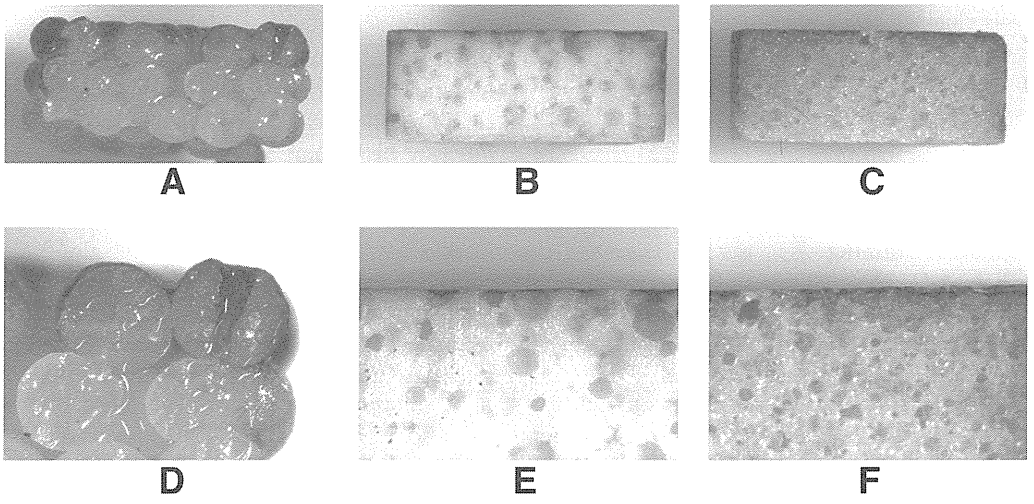

FIGURE 3. ALP staining of HA ceramic disks. Sagittal sectional view of MLPC (A and D), HA-A (B and E), HA-C (C and F).

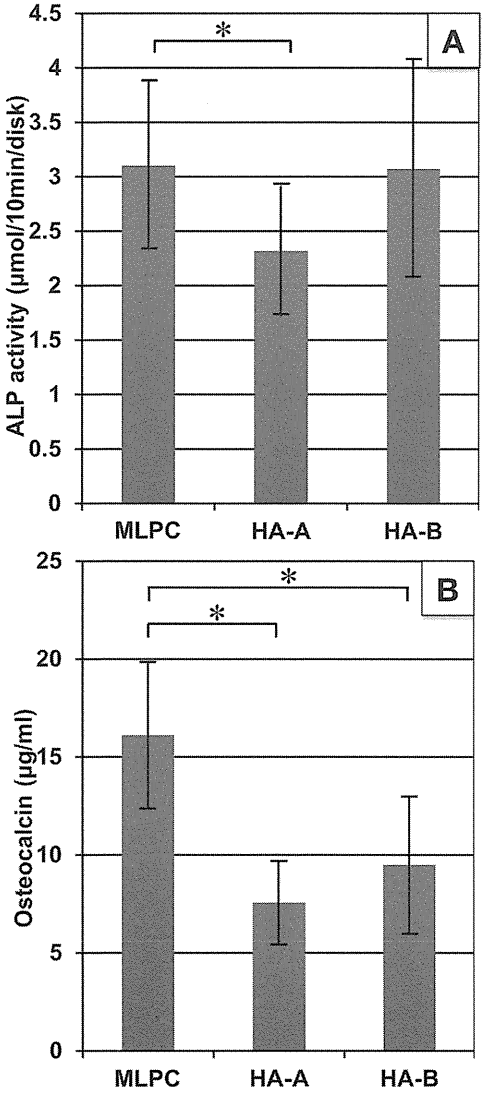

FIGURE 4. Quantification of osteoblastic markers *in vitro*. (A) ALP activity. Values are means ± SD (MLPC: $n = 6$, HA-A: $n = 9$, HA-B: $n = 9$). $^{*}P < 0.05$. (B) Osteocalcin secretion. Values are means ± SD (MLPC: $n = 11$, HA-A: $n = 12$, HA-B: $n = 12$). $^{*}p < 0.05$.

formation of ceramics/pore boundaries in the CT image, where the partial volume effect generates transitional voxel intensities.

Figure 5(A′–C′) shows μCT images of the disks after the *in vivo* test (A′: BMSCs/MLPC, B′: BMSCs/HA-A, and C′: BMSCs/HA-B). All the disks exhibited voxel intensity increases in the pores, indicating new bone formation. In the BMSCs/MLPC group, the increases were observed across the disk, and each portion showing an increase was thick and well-linked. The increase was evident on the voxel intensity histogram as a peak at an approximate voxel intensity of 39,800. In the other groups, increases were small and lacked continuity. In the BMSCs/HA-A group, the voxel intensity increase was observed on the surface of the disks [(Fig. 5(B′)]. In the BMSCs/HA-B group, voxel intensity increases were apparently widespread, but could not be detected on the voxel intensity histogram [(Fig. 5(C′)].

Histological analysis *in vivo*

Typical histological images are shown in Figure 6(A″–C″). In all cases, new bone formation was found along the surfaces of the disk and inside the pores; however, each group exhibited distinct characteristics. In the BMSCs/MLPC group, portions of the new bone were remarkably thick in the through-hole and gaps of the units and could be found relatively deep inside the disk [(Fig. 6(A″)]. In the BMSCs/HA-A group, new bone was mainly formed along the exofacial surface of the disks and the pores located just below the exofacial surface [(Fig. 6(B″)]. In the BMSCs/HA-B group, newly formed bone was seen on the surface and inside the disks [(Fig. 6(C″)]. However, portions of the new bone were small and infrequent, and their area was slightly smaller than that of the BMSCs/MLPC group. These histological findings were concordant with the micro CT findings.

Biochemical analysis *in vivo*

To quantify *in vivo* bone formation using the three different HA ceramics, we assessed the osteocalcin secretions of BMSCs on MLPC, HA-A, and HA-B after 6 weeks of subcutaneous implantation (Fig. 7). The mean osteocalcin content was 12.49 μg/mL in BMSCs/MLPC, 7.85 μg/mL in BMSCs/HA-A, and 7.93 μg/mL in BMSCs/HA-B. Figure 7 shows that the mean osteocalcin content of BMSCs/MLPC was highest among the three groups, and significant differences in the osteocalcin content were found between the BMSCs/MLPC and BMSCs/HA-A groups ($p < 0.05$), and between the BMSCs/MLPC and BMSCs/HA-B groups ($p < 0.05$).

DISCUSSION

In this study, we examined the osteogenic potential of MSCs on MLPC and two commercially available synthetic porous HA ceramics (HA-A and HA-B) both *in vitro* and *in vivo*. *In vitro*, the MSCs on MLPC group had the highest ALP activity and osteocalcin secretion among the three groups tested. They also had the highest osteocalcin content *in vivo* and showed extensive bone formation on the surface and inside the disks. These results can be considered in conjunction with the geometrical features of the macropores in the test pieces.

Pore shape of HA-A and HA-B was assumed to be approximately spherical, but include a wide variety and randomness of pore shapes. HA-B can be regarded as one of the more successful products achieving high porosity and pore connectivity. As compared with MLPC, HA-B is far superior in porosity, but the average pore size of HA-B is smaller. However, on the basis of histological observations, new bone formation inside HA-B was inferior to that of MLPC. Furthermore, while there were pores filled with new bone, they were a rather embolic phenomenon, isolated in pores in deeper positions. This result implies that high porosity of HA-B was disrupted by the pore geometries in HA-B, and the optimal pore size for osteoconduction remains to be defined.

Aside from pore size, the width of the connecting path of pores is also important and its design needs to be controllable. The connecting path is usually narrower than the pore itself and is therefore the limiting factor for fluid

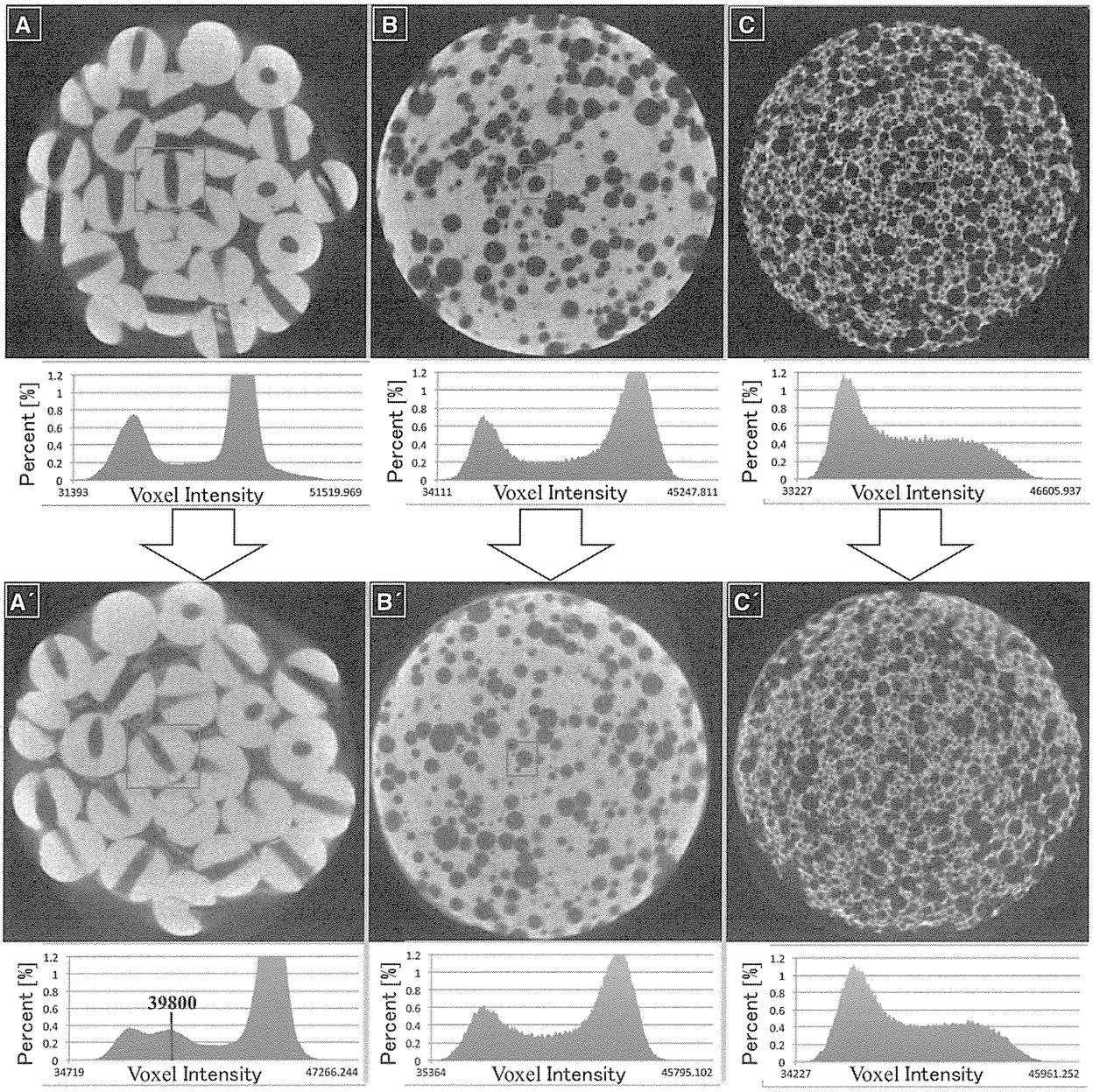

FIGURE 5. The μCT images of the disks with voxel intensity histograms (MLPC: A, A′; HA-A: B, B′; HA-B: C, C′). The μCT images A′-C′ are images after the *in vivo* test. Red squares on the μCT images indicate the region of interest (ROI). A peak attributable to new bone was evident in the voxel intensity histogram of MLPC. [Color figure can be viewed in the online issue, which is available at wileyonlinelibrary.com.]

FIGURE 6. Histological images of implant disks (H&E staining). Sagittal sectional view of MLPC: (A″), HA-A: (B″), and HA-B: (C″). Scale bar = 1 mm. [Color figure can be viewed in the online issue, which is available at wileyonlinelibrary.com.]